

# Direct Probe of Acceleration of PeV Electrons in the Crab Nebula

January 4, 2021

F. Aharonian<sup>26,27</sup>, Q. An<sup>4,5</sup>, Axikegu<sup>20</sup>, L.X. Bai<sup>21</sup>, Y.X. Bai<sup>1,3</sup>, Y.W. Bao<sup>15</sup>, D. Bastieri<sup>10</sup>, X.J. Bi<sup>1,2,3</sup>, Y.J. Bi<sup>1,3</sup>, H. Cai<sup>23</sup>, J.T. Cai<sup>10</sup>, Z. Cao<sup>1,2,3,\*</sup>, Z. Cao<sup>4,5</sup>, J. Chang<sup>16</sup>, J.F. Chang<sup>1,3,4</sup>, X.C. Chang<sup>1,3</sup>, B.M. Chen<sup>13</sup>, J. Chen<sup>21</sup>, L. Chen<sup>1,2,3</sup>, L. Chen<sup>18</sup>, L. Chen<sup>20</sup>, M.J. Chen<sup>1,3</sup>, M.L. Chen<sup>1,3,4</sup>, Q.H. Chen<sup>20</sup>, S.H. Chen<sup>1,2,3</sup>, S.Z. Chen<sup>1,3,†</sup>, T.L. Chen<sup>22</sup>, X.L. Chen<sup>1,2,3</sup>, Y. Chen<sup>15</sup>, N. Cheng<sup>1,3</sup>, Y.D. Cheng<sup>1,3</sup>, S.W. Cui<sup>13</sup>, X.H. Cui<sup>7</sup>, Y.D. Cui<sup>11</sup>, B.Z. Dai<sup>24</sup>, H.L. Dai<sup>1,3,4</sup>, Z.G. Dai<sup>15</sup>, Danzengluobu<sup>22</sup>, D. della Volpe<sup>31</sup>, B. D’Ettorre Piazzoli<sup>28</sup>, X.J. Dong<sup>1,3</sup>, J.H. Fan<sup>10</sup>, Y.Z. Fan<sup>16</sup>, Z.X. Fan<sup>1,3</sup>, J. Fang<sup>24</sup>, K. Fang<sup>1,3</sup>, C.F. Feng<sup>17</sup>, L. Feng<sup>16</sup>, S.H. Feng<sup>1,3</sup>, Y.L. Feng<sup>16</sup>, B. Gao<sup>1,3</sup>, C.D. Gao<sup>17</sup>, Q. Gao<sup>22</sup>, W. Gao<sup>17</sup>, M.M. Ge<sup>24</sup>, L.S. Geng<sup>1,3</sup>, G.H. Gong<sup>6</sup>, Q.B. Gou<sup>1,3</sup>, M.H. Gu<sup>1,3,4</sup>, J.G. Guo<sup>1,2,3</sup>, X.L. Guo<sup>20</sup>, Y.Q. Guo<sup>1,3</sup>, Y.Y. Guo<sup>1,2,3,16</sup>, Y.A. Han<sup>14</sup>, H.H. He<sup>1,2,3</sup>, H.N. He<sup>16</sup>, J.C. He<sup>1,2,3</sup>, S.L. He<sup>10</sup>, X.B. He<sup>11</sup>, Y. He<sup>20</sup>, M. Heller<sup>31</sup>, Y.K. Hor<sup>11</sup>, C. Hou<sup>1,3</sup>, X. Hou<sup>25</sup>, H.B. Hu<sup>1,2,3</sup>, S. Hu<sup>21</sup>, S.C. Hu<sup>1,2,3</sup>, X.J. Hu<sup>6</sup>, D.H. Huang<sup>20</sup>, Q.L. Huang<sup>1,3</sup>, W.H. Huang<sup>17</sup>, X.T. Huang<sup>17</sup>, Z.C. Huang<sup>20</sup>, F. Ji<sup>1,3</sup>, X.L. Ji<sup>1,3,4</sup>, H.Y. Jia<sup>20</sup>, K. Jiang<sup>4,5</sup>, Z.J. Jiang<sup>24</sup>, C. Jin<sup>1,2,3</sup>, D. Kuleshov<sup>29</sup>, K. Levochkin<sup>29</sup>, B.B. Li<sup>13</sup>, C. Li<sup>1,3</sup>, C. Li<sup>4,5</sup>, F. Li<sup>1,3,4</sup>, H.B. Li<sup>1,3</sup>, H.C. Li<sup>1,3</sup>, H.Y. Li<sup>5,16</sup>, J. Li<sup>1,3,4</sup>, K. Li<sup>1,3</sup>, W.L. Li<sup>17</sup>, X. Li<sup>4,5</sup>, X. Li<sup>20</sup>, X.R. Li<sup>1,3</sup>, Y. Li<sup>21</sup>, Y.Z. Li<sup>1,2,3</sup>, Z. Li<sup>1,3</sup>, Z. Li<sup>9</sup>, E.W. Liang<sup>12</sup>, Y.F. Liang<sup>12</sup>, S.J. Lin<sup>11</sup>, B. Liu<sup>5</sup>, C. Liu<sup>1,3</sup>, D. Liu<sup>17</sup>, H. Liu<sup>20</sup>, H.D. Liu<sup>14</sup>, J. Liu<sup>1,3</sup>, J.L. Liu<sup>19</sup>, J.S. Liu<sup>11</sup>, J.Y. Liu<sup>1,3</sup>, M.Y. Liu<sup>22</sup>, R.Y. Liu<sup>15</sup>, S.M. Liu<sup>16</sup>, W. Liu<sup>1,3</sup>, Y.N. Liu<sup>6</sup>, Z.X. Liu<sup>21</sup>, W.J. Long<sup>20</sup>, R. Lu<sup>24</sup>, H.K. Lv<sup>1,3</sup>, B.Q. Ma<sup>9</sup>, L.L. Ma<sup>1,3</sup>, X.H. Ma<sup>1,3</sup>, J.R. Mao<sup>25</sup>, A. Masood<sup>20</sup>, W. Mitthumsiri<sup>32</sup>, T. Montaruli<sup>31</sup>, Y.C. Nan<sup>17</sup>, B.Y. Pang<sup>20</sup>, P. Pattarakijwanich<sup>32</sup>, Z.Y. Pei<sup>10</sup>, M.Y. Qi<sup>1,3</sup>, D. Ruffolo<sup>32</sup>, V. Rulev<sup>29</sup>, A. Sáiz<sup>32</sup>, L. Shao<sup>13</sup>, O. Shchegolev<sup>29,30</sup>, X.D. Sheng<sup>1,3</sup>, J.R. Shi<sup>1,3</sup>, H.C. Song<sup>9</sup>, Yu.V. Stenkin<sup>29,30</sup>, V. Stepanov<sup>29</sup>, Q.N. Sun<sup>20</sup>, X.N. Sun<sup>12</sup>, Z.B. Sun<sup>8</sup>, P.H.T. Tam<sup>11</sup>, Z.B. Tang<sup>4,5</sup>, W.W. Tian<sup>2,7</sup>, B.D. Wang<sup>1,3</sup>, C. Wang<sup>8</sup>, H. Wang<sup>20</sup>, H.G. Wang<sup>10</sup>, J.C. Wang<sup>25</sup>, J.S. Wang<sup>19</sup>, L.P. Wang<sup>17</sup>, L.Y. Wang<sup>1,3</sup>, R.N. Wang<sup>20</sup>, W. Wang<sup>11</sup>, W. Wang<sup>23</sup>, X.G. Wang<sup>12</sup>, X.J. Wang<sup>1,3</sup>, X.Y. Wang<sup>15</sup>, Y.D. Wang<sup>1,3</sup>, Y.J. Wang<sup>1,3</sup>, Y.P. Wang<sup>1,2,3</sup>, Z. Wang<sup>1,3,4</sup>, Z. Wang<sup>19</sup>, Z.H. Wang<sup>21</sup>, Z.X. Wang<sup>24</sup>, D.M. Wei<sup>16</sup>, J.J. Wei<sup>16</sup>, Y.J. Wei<sup>1,2,3</sup>, T. Wen<sup>24</sup>, C.Y. Wu<sup>1,3</sup>, H.R. Wu<sup>1,3</sup>, S. Wu<sup>1,3</sup>, W.X. Wu<sup>20</sup>, X.F. Wu<sup>16</sup>, S.Q. Xi<sup>20</sup>, J. Xia<sup>5,16</sup>, J.J. Xia<sup>20</sup>, G.M. Xiang<sup>2,18</sup>, G. Xiao<sup>1,3</sup>, H.B. Xiao<sup>10</sup>, G.G. Xin<sup>23</sup>, Y.L. Xin<sup>20</sup>, Y. Xing<sup>18</sup>, D.L. Xu<sup>19</sup>, R.X. Xu<sup>9</sup>, L. Xue<sup>17</sup>, D.H. Yan<sup>25</sup>, C.W. Yang<sup>21</sup>, F.F. Yang<sup>1,3,4</sup>, J.Y. Yang<sup>11</sup>, L.L. Yang<sup>11</sup>, M.J. Yang<sup>1,3</sup>, R.Z. Yang<sup>5</sup>, S.B. Yang<sup>24</sup>, Y.H. Yao<sup>21</sup>, Z.G. Yao<sup>1,3</sup>, Y.M. Ye<sup>6</sup>, L.Q. Yin<sup>1,3</sup>, N. Yin<sup>17</sup>, X.H. You<sup>1,3</sup>, Z.Y. You<sup>1,2,3</sup>, Y.H. Yu<sup>17</sup>, Q. Yuan<sup>16</sup>, H.D. Zeng<sup>16</sup>, T.X.

Zeng<sup>1,3,4</sup>, W. Zeng<sup>24</sup>, Z.K. Zeng<sup>1,2,3</sup>, M. Zha<sup>1,3,†</sup>, X.X. Zhai<sup>1,3</sup>, B.B. Zhang<sup>15</sup>, H.M. Zhang<sup>15</sup>, H.Y. Zhang<sup>17</sup>, J.L. Zhang<sup>7</sup>, J.W. Zhang<sup>21</sup>, L. Zhang<sup>13</sup>, L. Zhang<sup>24</sup>, L.X. Zhang<sup>10</sup>, P.F. Zhang<sup>24</sup>, P.P. Zhang<sup>13</sup>, R. Zhang<sup>5,16</sup>, S.R. Zhang<sup>13</sup>, S.S. Zhang<sup>1,3</sup>, X. Zhang<sup>15</sup>, X.P. Zhang<sup>1,3</sup>, Y. Zhang<sup>1,3</sup>, Y. Zhang<sup>1,16</sup>, Y.F. Zhang<sup>20</sup>, Y.L. Zhang<sup>1,3</sup>, B. Zhao<sup>20</sup>, J. Zhao<sup>1,3</sup>, L. Zhao<sup>4,5</sup>, L.Z. Zhao<sup>13</sup>, S.P. Zhao<sup>16,17</sup>, F. Zheng<sup>8</sup>, Y. Zheng<sup>20</sup>, B. Zhou<sup>1,3</sup>, H. Zhou<sup>19</sup>, J.N. Zhou<sup>18</sup>, P. Zhou<sup>15</sup>, R. Zhou<sup>21</sup>, X.X. Zhou<sup>20</sup>, C.G. Zhu<sup>17</sup>, F.R. Zhu<sup>20</sup>, H. Zhu<sup>7</sup>, K.J. Zhu<sup>1,2,3,4</sup>, X. Zuo<sup>1,3</sup>, (The LHAASO Collaboration)

<sup>1</sup> Key Laboratory of Particle Astrophysics & Experimental Physics Division & Computing Center, Institute of High Energy Physics, Chinese Academy of Sciences, 100049 Beijing, China

<sup>2</sup>University of Chinese Academy of Sciences, 100049 Beijing, China

<sup>3</sup>TIANFU Cosmic Ray Research Center, Chengdu, Sichuan, China

<sup>4</sup>State Key Laboratory of Particle Detection and Electronics, China

<sup>5</sup>University of Science and Technology of China, 230026 Hefei, Anhui, China

<sup>6</sup>Department of Engineering Physics, Tsinghua University, 100084 Beijing, China

<sup>7</sup>National Astronomical Observatories, Chinese Academy of Sciences, 100101 Beijing, China

<sup>8</sup>National Space Science Center, Chinese Academy of Sciences, 100190 Beijing, China

<sup>9</sup>School of Physics, Peking University, 100871 Beijing, China

<sup>10</sup>Center for Astrophysics, Guangzhou University, 510006 Guangzhou, Guangdong, China

<sup>11</sup>School of Physics and Astronomy & School of Physics (Guangzhou), Sun Yat-sen University, 519000 Zhuhai, Guangdong, China

<sup>12</sup>School of Physical Science and Technology, Guangxi University, 530004 Nanning, Guangxi, China

<sup>13</sup>Hebei Normal University, 050024 Shijiazhuang, Hebei, China

<sup>14</sup>School of Physics and Microelectronics, Zhengzhou University, 450001 Zhengzhou, Henan, China

<sup>15</sup>School of Astronomy and Space Science, Nanjing University, 210023 Nanjing, Jiangsu, China

<sup>16</sup>Key Laboratory of Dark Matter and Space Astronomy, Purple Mountain Observatory, Chinese Academy of Sciences, 210023 Nanjing, Jiangsu, China

<sup>17</sup>Institute of Frontier and Interdisciplinary Science, Shandong University, 266237 Qingdao, Shandong, China

<sup>18</sup>Key Laboratory for Research in Galaxies and Cosmology, Shanghai Astronomical Observatory, Chinese Academy of Sciences, 200030 Shanghai, China

<sup>19</sup>Tsung-Dao Lee Institute & School of Physics and Astronomy, Shanghai Jiao Tong University, 200240 Shanghai, China

<sup>20</sup>School of Physical Science and Technology & School of Information Science and Technology, Southwest Jiaotong University, 610031 Chengdu, Sichuan, China

<sup>21</sup>College of Physics, Sichuan University, 610065 Chengdu, Sichuan, China

<sup>22</sup>Key Laboratory of Cosmic Rays (Tibet University), Ministry of Education, 850000 Lhasa, Tibet, China

<sup>23</sup>School of Physics and Technology, Wuhan University, 430072 Wuhan, Hubei, China

<sup>24</sup>School of Physics and Astronomy, Yunnan University, 650091 Kunming, Yunnan, China

<sup>25</sup>Yunnan Observatories, Chinese Academy of Sciences, 650216 Kunming, Yunnan, China

<sup>26</sup>Dublin Institute for Advanced Studies, 31 Fitzwilliam Place, 2 Dublin, Ireland

<sup>27</sup>Max-Planck-Institut für Kernphysik, P.O. Box 103980, 69029 Heidelberg, Germany

<sup>28</sup>Dipartimento di Fisica dell'Università di Napoli "Federico II", Complesso Universitario di Monte Sant'Angelo, via Cinthia, 80126 Napoli, Italy.

<sup>29</sup>Institute for Nuclear Research of Russian Academy of Sciences, 117312 Moscow, Russia

<sup>30</sup>Moscow Institute of Physics and Technology, 141700 Moscow, Russia

<sup>31</sup>Département de Physique Nucléaire et Corpusculaire, Faculté de Sciences, Université de Genève, 24 Quai Ernest Ansermet, 1211 Geneva, Switzerland

<sup>32</sup>Department of Physics, Faculty of Science, Mahidol University, 10400 Bangkok, Thailand

\*E-mail: caozh@ihep.ac.cn; chensz@ihep.ac.cn; linsj6@mail.sysu.edu.cn; zhangss@ihep.ac.cn; zham@ihep.ac.cn; licong@ihep.ac.cn; wangly@ihep.ac.cn; yinlq@ihep.ac.cn; Felix.Aharonian@mpi-hd.mpg.de; ryliu@nju.edu.cn.

**We report the discovery of the highest energy  $\gamma$ -ray photon ever detected from the Crab Nebula. The association of an air shower detected by the Large High Altitude Air Shower Observatory (LHAASO) with a primary 0.9 Peta-electronvolt ( $1 \text{ PeV} = 10^{15} \text{ eV}$ ) photon, is a crucial step towards the opening of the Ultra-High Energy (UHE) window in the spectrum of cosmic electromagnetic radiation. At lower energies, the spectrum measured by WCDA and KM2A, two independent detectors of LHAASO, are in good agreement with the previous reports of other groups. The extension of the energy spectrum to 1 PeV provides a direct probe of acceleration of PeV electrons. It provides the first model-independent evidence that the Crab operates as an extreme electron accelerator boosting the energy of electrons at the rate close to its theoretical limit. The PeV photons, combined with the data of synchrotron emission in the soft (MeV)  $\gamma$ -ray band, give precise information about the magnetic field and ultrarelativistic electrons inside the electron PeVatron.**

## Main text:

The Crab Nebula is a historical Supernova Remnant. Its appearance on Aug 24, 1054 A.D., has been recorded in Chinese Chronicles as a ‘guest star’ (1). It is the brightest representative of Pulsar Wind Nebulae, a class of extended nonthermal structures powered by the rotational energy of neutron stars through the formation and termination of ultra-relativistic electron-positron pulsar winds. Several remarkable discoveries made in astrophysics associate with the Crab Nebula and its pulsar. Here we report a new revelation linked to this unique object - the spectral energy distribution (SED) measured over 3.5 decades, from 0.5 Tera-electronvolt ( $1\text{TeV} = 10^{12}\text{ eV}$ ) to 1 Peta-electronvolt ( $1\text{ PeV} = 10^{15}\text{ eV}$ ) by a mega cosmic-ray facility, LHAASO, located at 4410 m above sea level in high mountains of the Sichuan province of China.

LHAASO is a dual-purpose complex of particle detectors (2, 3) designed for the study of cosmic rays and  $\gamma$ -rays in the sub-TeV to 1000 PeV energy range. Once an energetic extraterrestrial particle, proton, nucleus or photon, enters the Earth’s atmosphere, it initiates a cascade of relativistic particles (‘air shower’) consisting of hadrons, leptons, and photons. The LHAASO detectors record different components of air showers which are used to reconstruct the type, energy and arrival direction of the primary particle. Currently, operating at its half capacity, LHAASO demonstrates performance close to the anticipated sensitivity. The facility will be fully completed in 2021.

LHAASO consists of three arrays (see Sec. 1 of ‘Methods’). The key component of the facility is the one-square-km array (KM2A) composed of the surface scintillation counters and the under-surface muon detector array. KM2A is designed to detect and identify the type of the primary cosmic ray (CR) particles above 10 TeV to 100 PeV energies. Thanks to the very high power of suppression of the hadronic showers initiated by CR protons and nuclei, and the capability of reconstruction of the energy and arrival direction of showers with accuracy 15 to 20 percent and  $0.25^\circ$ , respectively, KM2A serves as an ideal UHE  $\gamma$ -ray telescope. Above 50 TeV, the sensitivity of KM2A outreaches the performance of the all current or planned ground-based  $\gamma$ -ray detectors by one order of magnitude.

Water Cherenkov Detector Array (WCDA) is another principal component of the LHAASO experiment. Three ponds of total area of  $0.08 \text{ km}^2$  are designed for extension of  $\gamma$ -ray studies down to energies significantly below 1 TeV, with an angular resolution as good as  $0.2^\circ$ . WCDA can provide effective surveys of galactic and extragalactic source populations, and an effective monitoring of transient phenomena like AGN flares and gamma-ray bursts. For the extended TeV  $\gamma$ -ray sources WCDA can provide deeper probes than the current Imaging Atmospheric Cherenkov Telescope (IACT) arrays. Finally, at PeV energies, WCDA can be used as a giant muon detector for improvement of the performance of separation of the electromagnetic and hadronic showers detected by KM2A. Currently, WCDA operates with an energy threshold below 500 GeV.

KM2A and WCDA are complemented by the Wide-Field-of-view Cherenkov Telescope Array (WFCTA) (4) consisting of 18 units designed for detection of the Cherenkov radiation emitted by air showers produced by primary cosmic rays with energy ranging from 0.1 to 1000 PeV. While the main goal of inclusion of WFCTA in the facility is the improvement of accuracy of measurements of the spectrum and the composition of cosmic rays around and beyond the knee, the complementary information provided by the Cherenkov light of the air showers can be quite helpful also in studies of PeV  $\gamma$ -rays. Presently, fourteen WFCTA telescopes are configured in a way to cover a  $32^\circ \times 112^\circ$  patch of the northern sky through which the Crab Nebula is passing every day. The observations with WFCTA started in September 2019 demonstrate good agreement with the designed performance.

On January 11th, 2020 at 17h59m18s UTC, the array has been hit by a giant air shower recorded by all the LHAASO detectors. The shower arrived from the direction of Crab Nebula and landed at the west part of KM2A. The footprint of the event shown in Fig.1, demonstrates that WCDA was also triggered., despite being 150 m away from the shower core. The shower arrived after midnight when eight WFCTA telescopes were operational. The Cherenkov radiation of the shower appeared in the FoV of Telescope No.10 and triggered it. The image is also shown in Fig.1. The detection of this event demonstrates the importance of the ‘multi-component’ detection approach adopted in the LHAASO design.

Using the 4996 particles recorded by 395 surface detectors and 15 muons recorded by 11 muon detectors of KM2A, the chance probability of this event to be misidentified as a  $\gamma$ -ray induced shower, is estimated as small

as 0.2%. Two independent ways of estimation of the shower energy by using the KM2A data and WFCTA data demonstrate perfect, within the statistical uncertainties, agreement:  $0.88 \pm 0.11$  PeV by KM2A and  $0.90^{+0.24}_{-0.18}$  PeV by WFCTA. This was the first highest energy (almost 1 PeV!) photon ever detected from an astronomical object.

In overall, 54 UHE  $\gamma$ -rays with energy exceeding 100 TeV have been detected during 11 months of operation of KM2A operating in less than half of its designed capacity. Above 1 PeV, we extrapolate the detection rate as a power-law with the differential index found at lower energies,  $\Gamma = 3$ . Using these observations, in Fig.2 we show the integral  $\gamma$ -ray detection rate, re-normalized for the nominal 1 km<sup>2</sup> array and for one hour exposure time of the Crab being within the FoV of KM2A (approximately 5.8 hours per day with zenith angle less than 40°). Above 100 TeV, it is about 0.1 event per hour and two orders of magnitude less frequent at 1 PeV. Thus if the power-law spectrum of the Crab would continue as power-law beyond 1 PeV, one should expect approximately 4 photons with energy exceeding 1 PeV to be detected over the 1-year continuous operation of KM2A. In Fig.2, we also show the detection rate of cosmic rays within a cone of 1° centred at the Crab position on the sky, both before and after the ‘muon cuts’. At energies above 50 TeV, the detection rate of  $\gamma$ -rays from the Crab exceeds the detection rate of the cosmic-ray induced background by an order of magnitude. The difference dramatically increases with energy achieving a factor of 300 at 1 PeV. Thus, even for a  $\gamma$ -ray source with flux as weak as 0.1 Crab, the detection of UHE  $\gamma$ -rays by KM2A proceeds in the background-free regime! Note that, in addition to the cosmic-ray induced background, one should also expect a generic  $\gamma$ -ray background contributed by the diffuse galactic  $\gamma$ -rays. The ratio depends on the hydrogen column density of the interstellar medium in the direction of the Crab,  $N_{\text{H}+\text{H}_2} \approx 3 \times 10^{21} \text{ cm}^2$ , and is estimated as  $J_\gamma/J_{\text{CR}} \approx 5 \times 10^{-5}$ . If at 100 TeV  $\gamma$ -rays are detected at a rate comparable to the cosmic-ray detection rate (after the ‘muon cuts’), at higher energies, in particular above 1 PeV, the background is dominated by the diffuse galactic  $\gamma$ -ray emission.

The spectral energy distribution (SED) of  $\gamma$ -rays measured by WCDA from 0.5 TeV to 13 TeV and by KM2A from 10 TeV to 1 PeV is shown in Fig.3. The good agreement between the flux measurements by two independent facilities of LHAASO around 10 TeV provides a self cross-check inside the LHAASO experiment. The results agree also with the ground-based measurements reported by other groups.

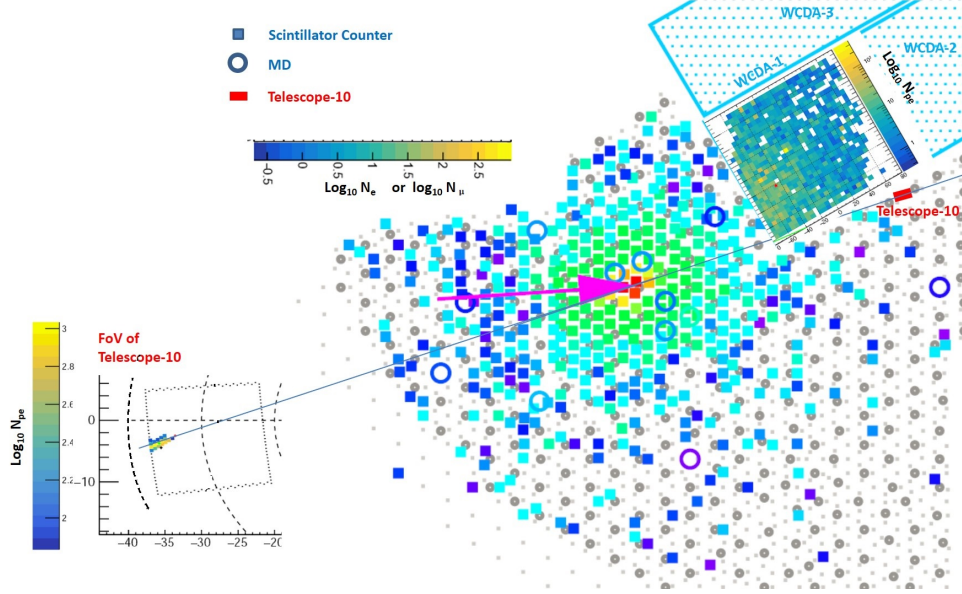


Figure 1: The footprint of the 0.9 PeV  $\gamma$ -ray event recorded by the LHAASO detectors from the direction of the Crab Nebula. The squares identify the scintillator counters of KM2A with the number of particles measured by the counters,  $N_e$ . The colour of each box illustrates the number of particles in the logarithm scale,  $\log_{10} N_e$ . In total, 4996 particles have been detected by 395 counters. The open circles represent 11 Muon Detectors of KM2A triggered by the shower, using the same colour convention. In total, 15 muons have been detected. The position of the core is indicated by the red arrow, which also illustrates the azimuth angle of the arrival direction of the primary  $\gamma$ -ray photon. At the distance of about 150 m from the shower core, is shown the WCDA detector; the triggered cells are highlighted. On the southern side of WCDA is located one of the wide FoV Cherenkov telescope, namely, the Telescope-10 that also detected the event. On the left side, the telescope FoV is illustrated by a square, while the dashed arcs indicate the zenith angles of 20°, 30°, 40°, from right to left. The shower image, composed by 15 pixels, started about 34° in zenith and stretched to the edge of FoV at 38°. In total, 9100 photoelectrons have been recorded by the telescope at the distance of 250 m from the shower core. The colour scale on the left side of the plot shows the logarithm of the number of photoelectrons in pixels. The line running through the telescope, shower core, and main axis of the image in the FoV of the telescope, demonstrates good agreement of the geometric measurements.

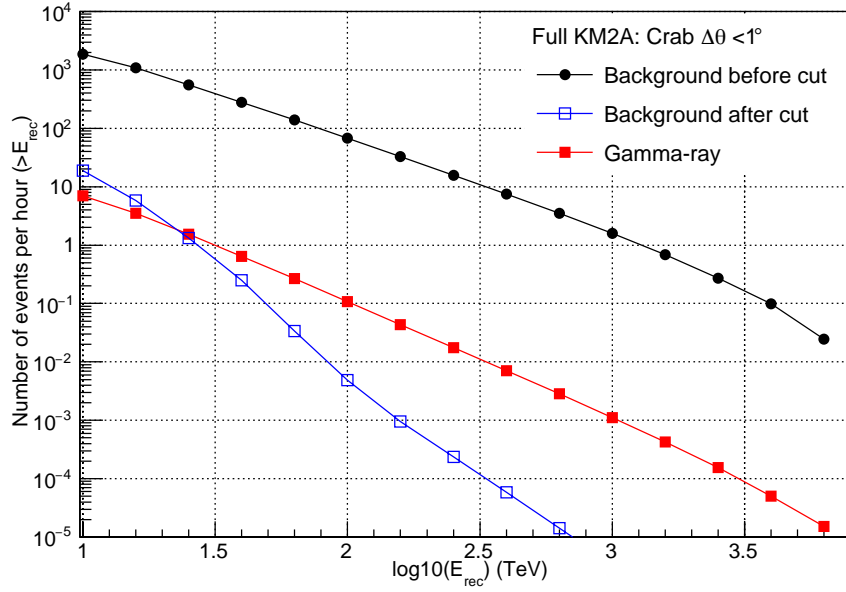


Figure 2: The rates of detection of  $\gamma$ -rays from the Crab Nebula and the cosmic ray induced background events above the shower energy  $E_{rec}$  by the  $1 \text{ km}^2$  array in a cone of  $1^\circ$  at the Crab direction. The rates correspond to the number of events per 1-hour of observations of the source being within the field-of-view of KM2A.  $E_{rec}$  is the energy obtained by the shower reconstruction algorithm. The red filled squares represent the number of gamma-rays as measured below 1 PeV and extrapolated to higher energies assuming the same power law. The black filled symbols represent the background cosmic ray events accumulated by KM2A. It is roughly a power law with the index of -1.6. The blue open symbols represent the integrated rate of cosmic ray events survived to the ‘muon cut’, namely the number of muons detected by KM2A in the shower must be less than about 1/200 of the number of particles detected by the KM2A surface counters. This cut is sufficient for the suppression of the cosmic ray background by the factors of 1,000 and 500,000 at 50 TeV and 1 PeV, respectively.



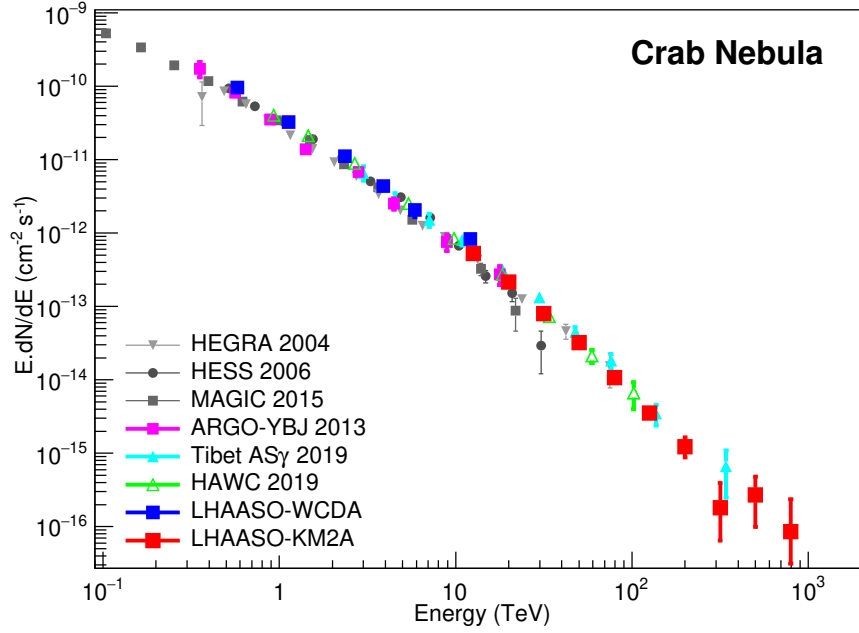


Figure 3: Very and ultra high energy  $\gamma$ -ray fluxes of the Crab Nebula. The LHAASO spectral points are shown together with the measurements of Atmospheric Cherenkov Telescope arrays: HEGRA (5), H.E.S.S. (6), MAGIC (7) and VERITAS (8), as well as of the air shower detectors ARGO-YBJ (9), HAWC (10) and Tibet AS $_{\gamma}$  (11). The red squares represent the measurements conducted during 308 days of operation of approximately 1/2 of the designed KM2A array. The purple squares are the spectral points measured during 123 days by approximately 30% of the designed area of the Water Cherenkov Detector Array (WCDA). The good agreement of the fluxes measured by two independent arrays of LHAASO at overlapping energies around 10 TeV provides cross-checking between two independent measurements with different techniques. The measurements above 100 TeV are essentially ‘background-free’, with 54 detected  $\gamma$ -rays versus only 1.5 event expected from the CR induced (hadronic) air showers survived after passing the ‘muon-poor’ cuts.

The Crab Nebula is a unique cosmic laboratory. Its radiation, after the new LHAASO results, spans over 22 decades, from MHz radio to UHE  $\gamma$ -rays. The emission has a nonthermal origin dominated by two mechanisms - the synchrotron radiation and Inverse Compton (IC) scattering of relativistic electrons interacting with the ambient magnetic and radiation fields. According to the standard paradigm, the nebula is powered by the relativistic electron-positron wind originating at the pulsar and terminated by the standing reverse shock at the distance from the pulsar  $R \approx 0.1$  pc (12, 13). The acceleration of electrons is associated with the termination of the wind but the details, including the acceleration mechanism(s), remain highly unknown. Nevertheless, the very fact of detection of the photon of  $\approx 1$  PeV allows us to estimate the acceleration rate presented in the general form  $\eta e B c$ . The parameter  $\eta$  representing the ratio of the projection of the electric field, averaged over the particle trajectory, to the magnetic field,  $\eta = E_{\text{eff}}/B \leq 1$ , characterizes the acceleration efficiency. The factories of relativistic particles with  $\eta \rightarrow 1$  implying the maximum acceleration rate allowed by classical electrodynamics, are called Extreme Accelerators (14). Remarkably, the so-called ‘Hillas diagram’ based on the condition of  $r_L = R$ , where  $r_L = E/eB$  is the particle Larmor radius, and  $R$  is the size of the source, does imply an Extreme Accelerator ( $\eta = 1$ ) but ignores the energy losses of particles during the acceleration. In any realistic scenario, the balance between the acceleration and the synchrotron loss rates gives more stringent constrain on the maximum energy achievable by the electron:

$$E_{\text{e,max}} = 5.8\eta^{1/2}(B/100\mu\text{G})^{-1/2} \text{ PeV} . \quad (1)$$

In the Crab Nebula, several radiation fields supply target photons for the IC scattering of electrons. However, at energies above 100 TeV, the 2.7 K CMBR remains the only significant contributor to the  $\gamma$ -ray production (15). Given the precise information about 2.7 K CMBR, the  $\gamma$ -ray data provide a direct, model-independent information about the parent electrons. The  $\gamma$ -ray production above 100 TeV proceeds in the Klein-Nishina regime where the ratio  $E_\gamma/E_e$  gradually approaches to 1. For the most energetic photon detected from the Crab,  $E_\gamma \approx 0.9$  PeV, the energy of the electrons should be approximately 2 PeV. The simultaneous modelling of the the synchrotron and IC components of the broadband emission constraints the magnetic field strength within a narrow ( $\delta B/B \leq 10\%$ ) interval around  $B = 115\mu\text{G}$  (See Sec.3 of ‘Methods’). Then, from Eq. (1) follows that the acceleration proceeds

at an incredibly high rate characterized by  $\eta \geq 0.1$ . For comparison, at the Diffusive Shock Acceleration in Supernova Remnants (16),  $\eta$  is by at least two orders of magnitude smaller.

Does the detection of  $\geq 100$  TeV photons agree with theoretical predictions within the standard paradigm of the Crab Nebula (15, 17–20)? We modelled the MWL radiation based on a few underlying assumptions (see Sec.3 in ‘Methods’). Within the one-zone model, the IC  $\gamma$ -ray spectrum at ultra-high energies can be calculated with high precision. Because of the Klein-Nishina effect, the  $\gamma$ -ray spectrum suffers gradual steepening with an average photon index  $\Gamma \approx 3.5$  between 100 TeV–1 PeV, and severe suppression above 1 PeV. While the LHAASO measurements do agree, within the statistical uncertainties, with the predicted spectrum, the points above 300 TeV show a tendency of hardening, instead of the anticipated steepening (see Fig.4). Whether the deviations of the spectral points from the theoretical prediction are the result of statistical fluctuations or they imply an inconsistency with the one-zone model, the data to be accumulated over the coming years can give a definite answer to this question. Indeed, two-year Crab observations (approximately 4000-hour exposure) with the fully completed KM2A should increase the background-free photon statistics by one order of magnitude, which should be sufficient to reveal any significant spectral feature between 100 TeV and 1 PeV. While it is the matter of time to settle this issue, below we briefly discuss two possible channels of highest energy  $\gamma$ -rays on top of the standard IC spectrum.

The dramatic suppression of the IC emissivity well above 100 TeV can be circumvented by introducing a second population of PeV electrons. Actually, a two-electron components model has been proposed while ago (21) to address the flattening of the Crab spectrum at energies 1 – 10 MeV (22), after the tendency of steepening of the synchrotron X-ray spectrum. Recently, the idea of co-existence of two distinct electron populations in the Crab, accelerated presumably in different sites by different mechanisms, have been explored (20, 23), in particular in the context of continuation of the IC  $\gamma$ -ray spectrum to 1 PeV (20).

In Fig.4 we show the synchrotron and IC radiation spectra calculated for two electron distributions: (i) the first power-law component with super-exponential cutoff,  $E^{-\alpha} \exp[-(E/E_0)^2]$  with  $E_0 = 2.45$  PeV,  $\alpha = 1.69$  for  $E < 0.64$  TeV and  $\alpha = 3.37$  for  $E \geq 0.64$  TeV; (ii) the second component with Maxwellian type distribution,

$E^2 \exp[-E/E_2]$  with  $E_2 = 240$  TeV. Note that the Maxwellian distribution does not imply a thermal equilibrium; it is just a convenient presentation form of a class of narrow distributions characterizing, in particular, the spectra of particles accelerated at the magnetic reconnection (24, 25).

The synchrotron cooling limits the characteristics distance at which the highest energy electrons release all their energy:  $l_{\text{rad}} \leq 6 \times 10^{17} (E_e/1\text{PeV})^{-1} (B/100\mu\text{G})^{-2}$  cm. The multiwavelength modelling of the synchrotron and IC components of radiation does not allow a significant deviation of the average magnetic field from  $100\mu\text{G}$  implying that both the acceleration and radiation of PeV electrons take place in a compact region(s), attached, presumably, to the wind termination site. The short lifetime of electrons and their confinement in compact regions allow flux variability in both channels - IC  $\gamma$ -rays at PeV and Synchrotron radiation at MeV energies on timescales of months. The synchrotron radiation could show variability also on shorter timescales caused, e.g. due to the "synchrotron burning" of electrons in locations with suddenly enhanced, up to 1 mG magnetic field. Interestingly, this could initiate the so-called *Crab flares*, the spectacular variations of the MeV/GeV  $\gamma$ -ray fluxes frequently recorded on timescales of days (see the review (26) and references therein). At the presence of such a large magnetic field, the IC  $\gamma$ -ray component would be severely suppressed since the energy of relativistic electrons is predominantly channelled into the synchrotron radiation.

Although the two-zone model can produce a flat structure around 1 PeV, Eq.(1) demands a sharp cutoff in the IC spectrum around or slightly higher 1 PeV. Therefore, in the case of detection of  $\gamma$ -rays well beyond 1 PeV, one should invoke a new component of radiation, e.g. due to the interactions of relativistic protons with the ambient gas. The current pulsar wind paradigm gives a self-consistent explanation of the entire range of electromagnetic spectrum of the Crab Nebula from MHz radio waves to multi-hundred TeV photons. Yet,  $\gamma$ -radiation of hadronic origin has been proposed in the literature as an additional or alternative component to the IC  $\gamma$ -rays (21, 28–30). In Fig.4, is shown the SED of  $\pi^0$ -decay  $\gamma$ -rays calculated for the power-law distribution of protons with an index  $\alpha = 2$  and exponential cutoff at  $E_{p,0} = 100$  PeV. Given the distance to the Crab of 2 kpc, and the average nebular gas density of about  $5 \text{ cm}^{-3}$ , a rather modest, less than  $W_p = 10^{48}$  erg energy contained in accelerated protons is needed to provide detectable  $\gamma$ -ray fluxes above 1 PeV. This constitutes only one per cent of the rotational energy

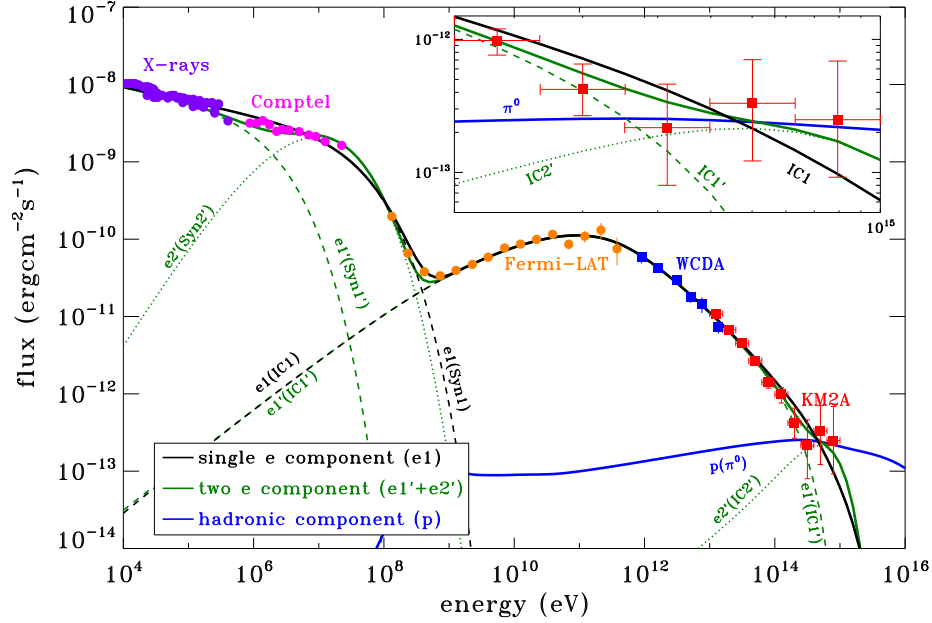


Figure 4: The Spectral Energy Distribution of the Crab Nebula. The black curves represent the fluxes of the Synchrotron (Syn1) and IC (IC1) components of radiation of the single electrons population (e1) calculated within the one-zone model. The electron spectrum is assumed to be a broken power-law function terminated by an super-exponential cutoff at the high-energy end. The model parameters for the electron spectrum are:  $\alpha_1 = 1.69$ ,  $\alpha_2 = 3.37$ ,  $E_b = 0.64$  TeV,  $E_0 = 2.45$  PeV. The total energy in electrons and the strength of the magnetic field are,  $W_e = 6.25 \times 10^{48}$  erg, and  $B_0 = 115 \mu\text{G}$ , respectively. The green curves show the fluxes of radiation by two electron populations. In this case, the first electron population (e1'), the radiation of which is shown by the dashed green curves (Syn1' and IC1'), is the same as the single electron population in the one-zone model except for the smaller cutoff energy,  $E_0 = 0.5$  PeV. The second electron population (e2') has a Maxwellian-type distribution with  $W_{e,2} = 1.5 \times 10^{44}$  ergs,  $B_2 = 100 \mu\text{G}$ ,  $E_2 = 0.24$  PeV. The radiation components of the second electron component (Syn2' and IC2') are presented by the dotted green curves. The contribution from a hypothetical hadronic component (p) shown with the solid blue curve, is calculated for the total energy in protons  $W_p = 6 \times 10^{47}$  ergs,  $n = 5 \text{ cm}^{-3}$ , the energy spectrum with the power-law spectral index  $\alpha_p = 2.0$ , and the cutoff  $E_{p,0} = 100$  PeV. The inserted figure in the top right corner zooms the fluxes above 100 TeV. The purple and the magenta circles show the X-ray and the MeV emission of the Crab Nebula (22). The orange circles represent Crab observations by Fermi-LAT in the non-flare state (27). The blue and red squares represents WCD and KM2A measurement reported in this work.

of the Crab pulsar released through the wind in the nebula over  $\approx 10^3$ yr. Unlike the IC component, the high energy break in the spectrum of the hadronic component of radiation is not strongly constrained. Thus, any detection of  $\gamma$ -rays beyond a few PeV would indicate to the presence of relativistic protons and nuclei in the nebula.

The continuation of observations of the Crab Nebula by LHAASO detectors over the next 2-3 years should give definite answers on the origin of PeV  $\gamma$ -rays, thus providing crucial information about the nature of the enigmatic Extreme Accelerator operating at the heart of this fascinating object.

## **Supplementary materials**

### **Materials and methods**

## **1 Experiment Description**

Large High Altitude Air Shower Observatory (LHAASO) (2) is a complex of extensive air shower (EAS) detectors installed on Mt. Haizi (29°21'27.6" N, 100°08'19.6" E) at 4410 m above sea level, in Sichuan province, China.

### **1.1 KM2A**

The array consisting of 5195 scintillator counters on the surface and 1188 underground muon detectors spread out over a circular area of 1.3 km<sup>2</sup>, is called KM2A. The details of these detectors and their operation are described elsewhere (31).

### **1.2 Water Cherenkov Detector Array**

At the center of the LHAASO array, the Water Cherenkov Detector Array (WCDA), composed of 3 large ponds, is one of the major components for the gamma ray astronomy in the LHAASO experiment. The first pond of 150 m × 150 m, equipped with 900 8-inch photomultiplier tubes (PMT) arranged on a square grid with a side of 5 m at 4.4 m beneath the water surface, has been used for the all sky survey observation since April 2019. The detector, which is active everywhere in the whole area, collect strong Cherenkov light signals generated by shower particles in water. The total amount of Cherenkov photons are proportional to energies carried by the particles, except for the muons, traversing the water. Well calibrated PMTs at the centers of 5 m × 5 m cells measure both number of photons and their arrival time. The PMTs are synchronized/calibrated within 0.2 ns. This enables the shower arrival direction to be measured with a resolution of 0.2° above a few TeV. Muons generate significantly stronger signals than other particles given the long track they produce, being more penetrating in water. Because the electrons/positrons and gamma rays laterally extend in space following a rather steep distribution function, at certain distance, e.g. 45 m from the shower center, density of those particles drops very low and muon signals become outstanding, thus the absence of those hot spots in the shower footprints at far distance works as an indication of electromagnetic

cascade showers induced by original gamma rays. In this way, the cosmic ray background could be suppressed at least by a factor of 100, and this enables a gamma ray source survey sensitivity of 65 milli-Crab-unit, more quantitatively, any source having an energy flux stronger than  $4 \times 10^{-13} \text{ erg/cm}^2\text{s}$  above 3 TeV will be detected by WCDA-1 with  $5 \sigma$  in a year. Up to now, the significance of  $77.4 \sigma$  for the Crab Nebula detection for 10 months confirmed that the sensitivity has been achieved by WCDA-1. The corresponding Spectral Energy Distribution (SED) of the Crab Nebula is measured using latest data set as shown in Fig. 2. More detailed description about the measurements of the SED is available elsewhere (32).

The second pond, having the same size as the first one, have been built and put in operation since January 2020. The detector is equipped with a 20" PMT plus a 3" PMT in each cell. This enhances the sensitivity at energies below 500 GeV, thus improved the performance of WCDA as a survey facility for transient phenomena such as gamma ray bursts. The third pond of  $110\text{m} \times 300\text{m}$  will be in operation at beginning of 2021. The total active area of WCDA will add up to be  $78,000 \text{ m}^2$ .

### **1.3 Wide FoV Cherenkov Telescope Array and the observation of showers**

8 Cherenkov telescopes, each of them covering a field of view (FoV) of  $16^\circ \times 16^\circ$ , have been operated for cosmic ray observation since October 2019. Showers hitting the LHAASO array falling within the FoV of telescopes will be recorded simultaneously. In order to efficiently carry out the coincident measurement, telescopes are located at the central region of the array, namely 6 of them are installed at the south-west corner and other 2 are at south-east corner of WCDA-1 as indicated in Fig.1. Seven telescopes are set to cover a zenith angle range from  $22^\circ$  to  $38^\circ$ , while one telescope is pointing up right. For the showers detected by telescopes, coincidence with WCDA or KM2A, the arrival direction is reconstructed with a precision of  $0.2^\circ$  and the core location on ground with an accuracy of 2 m. The precise geometric information allows the telescope to clearly calculate how many Cherenkov photons generated at various depth in the atmosphere since the shower started a few kilometers or even 20 kilometers above the telescope. In this way, the atmosphere above the telescope just like a conventional calorimeter for high energy particle experiments. As long as the sky is clear, the Cherenkov light, mainly near



ultraviolet photons, can be recorded no matter how high they were produced in air. Depending on the arrival direction of photons, an image is formed on a part of the camera, which is installed at the center of focal plane of the telescope and equipped with 1024 pixels. Each pixel, made of  $15\text{mm} \times 15\text{mm}$  SiPM, can measure the number of photons with good linear response over a wide range from 10-30,000. Adding up the number of photons over all registered pixels is an integration of the shower development profile represented by the number of Cherenkov photons generated by the charged shower particles. The brightness of the image turns out to be an estimator of the shower energy after correcting for a moderate effect on the distance between the telescope and the core location on the ground array, as the brightness decreases with the distance from the core. The shower energy is reconstructed by establishing a response function between the corrected total number of photons and the primary energy of the incident particle using a detailed Monte Carlo simulation which models the shower physics, its development in the atmosphere, the Cherenkov photon production and propagation, but also the telescope responses as the photons entered in the instrument.

Finally, the reconstructed energies of showers need to be calibrated for the absolute energy scale. The calibration has been done essentially by comparing energies with the ones reconstructed using WCDA on a group of commonly triggered events. As the matter of fact, WCDA absolute calibration was performed by measuring the deflection of the Moon shadows in geomagnetic field in the energy range from 6 TeV to 40 TeV as reported elsewhere (?).

## 2 Observation of the highest energy gamma ray and SED of the Crab Nebula

In the local coordinate system, this event arrived with a zenith angle of  $(33.9 \pm 0.2)^\circ$  according to the shower front reconstructed by the 395 registered scintillator counters, which are synchronized within 0.2 nanosecond, at about 2 am on January 12th, 2020 (Beijing time). Fig.S2 show the significance map around Crab Nebula region. A clear signal at  $6.2 \sigma$  is observed at energy above 400 TeV. The 0.9 PeV event is found just  $0.21^\circ$  away from the celestial coordinates of the Crab Nebula, as illustrated in Fig.S2. It is evident that this 0.9 PeV event is from the

Crab Nebula direction.

There is still great chance that the event has no connection at all with the Crab Nebula if it can not be identified as a gamma-like event. Here, the muon detector (MD) array works as a veto as described in Method of Ref. (31). Namely, the number of measured 15 muons ( $N_\mu$ ) versus the total number of particles measured by all counters ( $N_e$ ), 4996, indicates a very small muon content in this event. The probability of being a hadron induced shower, with such a small muon content, has been evaluated by counting how many events having the ratio of  $N_\mu/N_e$  less than the ratio of 15/4996. It is found only a few showers out of 12.3 million cosmic ray samples recorded by KM2A with  $E_{rec} \geq 0.88$  PeV. This estimates the chance probability of any single event to be recognized as a gamma event of  $6.7 \times 10^{-6}$ , as illustrated in Fig.S3. Only events coming from zone  $12^\circ$  away from the galactic plane are considered, to exclude any contribution from our galaxy. Taking into account that the Crab transients have specific occupancy of different zenith angles, this probability has been tested using events in 3 ranges, i.e.  $0^\circ$ - $20^\circ$ ,  $20^\circ$ - $40^\circ$  and  $20^\circ$ - $50^\circ$  and a negligible difference was found. Therefore, to be conservative, the probability is assumed to be  $10^{-5}$ . In the direction of the Crab Nebula, KM2A totally recorded 179 events with an angular distance from Crab Nebula less than  $0.3^\circ$ , which is slightly larger than the radius of the PSF of KM2A above 500 TeV. Using the probability given above, the number of expected background CR events is 0.00179. In other words, the chance probability of this event was not a photon is 0.179%.

One of the air Cherenkov telescopes, Telescope 10, pointing at a zenith angle of  $30^\circ$  and nearly at west saw the shower image at almost half-way from the center of its FoV at  $33.9^\circ$ . Since it is quite far from the telescope, the image was not very much extended, with only 15 pixels had signals above the threshold. However, the image is quite bright in terms of total number of photoelectrons in the image, which was 9,100. In order to understand this fascinating event, about 10,000 gamma ray induced showers with the same geometric parameters are simulated in a narrow energy range around 1 PeV. The generated showers precisely reproduced the footprint on KM2A, WCDA and the image in the telescope. The most probable energy among the simulated with  $9100 \pm 100$  photoelectrons in their images found to be  $0.90^{+0.24}_{-0.18}$  PeV.

The 395 scintillator counters measured the lateral distribution of the 5,476 secondary particles in the shower.

The core is reconstructed by fitting the distribution with the modified NKG functional form,  $N\Gamma(4.5 - s)/\Gamma(s - 0.5)/\Gamma(5 - 2s)(r/R_M)^{s-2.5}(1 + r/R_M)^{s-4.5}$ , where  $N$  is the total number of secondary particles in the shower,  $s$  is the shower age parameter, and  $R_M$  is the Moliere unit of 136 m as a measure of the width of the distribution at the altitude, and  $r$  is the perpendicular distance from the detector to the shower axis. The error of the core location is about 3 m. Here, the particles density at 50 m from the core determined in the fitting has been used as the energy estimator and has resulted in the shower energy of  $0.88 \pm 0.11$  PeV by assuming the primary particle a gamma photon.

The SED of Crab Nebula below 20 TeV was measured using data collected by WCDA-1 from September 2019 to February 2020, with the detector running quite stable with high duty cycle. The total exposure of the Crab Nebula in this period of time was 992 hours. The great details about the measurement have been reported elsewhere (32). The totally independent data set from December 2019 to November 2020, about 308 live days and 2236 hours for the Crab Nebula, collected by the 1/2 KM2A array has been used to measure the SED of the Crab Nebula above 10 TeV. The great details about the measurement have been reported else where (33). Here, only the SED above 0.1 PeV are discussed. Selected gamma ray events according to the ratio  $\log_{10}((N_\mu + 0.0001)/N_e)$  are picked around the Crab Nebula in a cone of  $0.4^\circ$  centered at the Crab Nebula to guarantee that 90% of signals inside the Point-Spread-Function (PSF) are contained. Since the energy resolution is found about 15%, one decade of energy is divided into 5 bins with a bin width of  $\Delta \log_{10} E = 0.2$ . In the operation of KM2A, we found 35, 13, 2, 3, 1 events in the 5 bins above 0.1 PeV, respectively. Subtracting the number of background CR events estimated by using direct-integration method for each bin, the flux is measured for each bin as a function of  $E$ , as presented in Fig.3. Much more details about the SED measurements can be found elsewhere (33).

Above 400 TeV, the Crab Nebula has been detected with the significance of  $6.2 \sigma$ . The sky map around Crab is shown in Fig. S2. The highest energy event at 0.9 PeV is marked as the star for its arrival direction.

### 3 Spectrum fitting

We assume a broken-power-law function with a super-exponential high-energy cutoff for the electron spectrum, i.e.,

$$\frac{dN}{dE_e} = N_0 E_e^{-\alpha_1} [1 + (E_e/E_c)^{\alpha_2 - \alpha_1}]^{-1} \exp[-(E_e/E_0)^2] \quad (\text{S1})$$

where  $\alpha_1$  and  $\alpha_2$  are the spectral indices before and after the spectral break,  $E_c$  is the break energy,  $E_0$  is the cutoff energy.  $N_0$  is the normalization factor which can be determined once the total energy in the electron spectrum  $W_e$  is given, via  $W_e = \int E_e \frac{dN}{dE_e} dE_e$ .

Electrons radiate in the magnetic field via the synchrotron radiation process and in the radiation field via the inverse Compton (IC) scattering. For a turbulent magnetic field with Gaussian distribution of an average strength  $B$ , we follow the interstellar radiation field modeled in Ref. (34), a far-infrared radiation excess from the nebula with a temperature of 70 K and an energy density of  $0.5 \text{ eV cm}^{-3}$ , and the synchrotron radiations. The latter one is assumed homogeneously generated within the nebula of a radius of 1.8 pc, and the volume-averaged photon density is enhanced by a factor of 2.24 with respect to the boundary of the nebula, following the treatment of in Ref. (15). We then scan the parameter space with evaluating the goodness of fit by the Pearson's chi-squared test.

Note that, for IC scattering on an isotropic target photon field of blackbody/greybody distribution, the relation between the energy of electron and average energy of up-scattered photons  $\bar{E}_\gamma$  can be described by a simple formula (35), i.e.

$$\frac{\bar{E}_\gamma}{E_e} = \frac{4E_e T}{4E_e T + 0.3 \log(1 + 4E_e T)} \quad (\text{S2})$$

where the energies of electron, up-scattered photons and temperature of the target photon are all expressed in unit of  $m_e c^2$ . For the 2.7K radiation field, it requires 1.9 PeV electron to produce 0.9 PeV photon as shown in Fig. S5.

The maximum electron energy needs to achieve 2 PeV in the modelling with a single electron component. There could be a second electron component accelerated in the nebula, for example, in the wisps or filaments which may indicate strong magnetic turbulence. In this case, a Maxwellian-type electron component, which may be accelerated by the magnetic reconnection process or the second-order Fermi process, is introduced following

Ref. (21), i.e.,

$$\frac{dN_2}{dE_e} = N_2 E_e^2 \exp(-E_e/E_2) \quad (\text{S3})$$

where  $N_2$  is again determined by a given total energy  $W_{e,2}$  for this component.  $E_2$  is the cutoff energy representing the maximum energy accelerated. Note that, for electrons of Maxwellian-type distribution, the radiation spectral cutoff is determined by the “temperature” which is  $E_T = 3E_2$ . As a consequence, it could relax the requirement on the maximum accelerated electron energy compared to the case of a power-law cutoff spectrum. We assume that the second component electron could radiate in a separated magnetic field  $B_2$  but the target radiation for the IC scattering is assumed to be the same with that of the first component.

If the magnetic field related to the second electron component is large, its IC radiation would be suppressed although its synchrotron radiation could still be consistent with the MeV – GeV data with employing a smaller  $E_2$ . Another possible contribution to the highest energy photons is the hadronic emission produced by the interaction between protons accelerated in the nebula and the matter therein. We assume the proton spectrum follow the form

$$\frac{dN_p}{dE_p} = N_{0,p} E_p^{-2} \exp(-E_p/E_{p,0}) \quad (\text{S4})$$

with a total energy  $W_p$  above 1 GeV which then determines the normalization factor  $N_{0,p}$ . We follow a semi-analytical method given by Ref. (36) to calculate the hadronic gamma-ray radiation.

**Acknowledgments** The authors would like to thank all staff members who work at the LHAASO site above 4400 meter above the sea level year round to maintain the detector and keep the water recycling system, electricity power supply and other components of the experiment operating smoothly. We are grateful to Chengdu Management Committee of Tianfu New Area for the constant financial supports to the researches with LHAASO data. This research work is also supported by following grants. The National Key R&D program of China under the grant 2018YFA0404201, 2018YFA0404202 and 2018YFA0404203, it also is supported by the National Natural Science Foundation of China (NSFC grants 11635011, 11761141001), ...

## References

1. K. Lundmark, *PASP* **33**, 225 (1921).
2. Z. Cao, *Chinese Physics C* **34**, 249 (2010).
3. H. He, *Radiation Detection Technology and Methods* **2**, 7 (2018).
4. WFCTA's observation on Crab .
5. F. Aharonian, *et al.*, *ApJ* **614**, 897 (2004).
6. F. Aharonian, *et al.*, *A&A* **457**, 899 (2006).
7. J. Aleksić, *et al.*, *Journal of High Energy Astrophysics* **5**, 30 (2015).
8. K. Meagher, VERITAS Collaboration, *34th International Cosmic Ray Conference (ICRC2015)* (2015), vol. 34 of *International Cosmic Ray Conference*, p. 792.
9. B. Bartoli, *et al.*, *ApJ* **798**, 119 (2015).
10. A. U. Abeysekara, *et al.*, *ApJ* **881**, 134 (2019).
11. M. Amenomori, *et al.*, *Phys. Rev. Lett.* **123**, 051101 (2019).
12. M. J. Rees, J. E. Gunn, *MNRAS* **167**, 1 (1974).
13. C. F. Kennel, F. V. Coroniti, *ApJ* **283**, 694 (1984).
14. F. A. Aharonian, A. A. Belyanin, E. V. Derishev, V. V. Kocharovskiy, V. V. Kocharovskiy, *Phys. Rev. D* **66**, 023005 (2002).
15. A. M. Atoyan, F. A. Aharonian, *MNRAS* **278**, 525 (1996).
16. M. A. Malkov, L. O. Drury, *Reports on Progress in Physics* **64**, 429 (2001).
17. O. C. de Jager, *et al.*, *ApJ* **457**, 253 (1996).
18. D. Volpi, L. Del Zanna, E. Amato, N. Bucciantini, *A&A* **485**, 337 (2008).

19. M. Meyer, D. Horns, H. S. Zechlin, *A&A* **523**, A2 (2010).
20. D. Khangulyan, M. Arakawa, F. Aharonian, *MNRAS* **491**, 3217 (2020).
21. F. A. Aharonian, A. M. Atoyan, *Neutron Stars and Pulsars: Thirty Years after the Discovery*, N. Shibasaki, ed. (1998), p. 439.
22. L. Kuiper, *et al.*, *A&A* **378**, 918 (2001).
23. M. Lyutikov, *et al.*, *MNRAS* **489**, 2403 (2019).
24. L. Sironi, A. Spitkovsky, *ApJ* **783**, L21 (2014).
25. B. Cerutti, G. R. Werner, D. A. Uzdensky, M. C. Begelman, *ApJ* **770**, 147 (2013).
26. R. Bühler, R. Blandford, *Reports on Progress in Physics* **77**, 066901 (2014).
27. M. Arakawa, M. Hayashida, D. Khangulyan, Y. Uchiyama, *arXiv e-prints* p. arXiv:2005.07958 (2020).
28. K. S. Cheng, T. Cheung, M. M. Lau, K. N. Yu, P. W. Kwok, *Journal of Physics G Nuclear Physics* **16**, 1115 (1990).
29. W. Bednarek, R. J. Protheroe, *Phys. Rev. Lett.* **79**, 2616 (1997).
30. X. C. Yang, L. Zhang, *A&A* **496**, 751 (2009).
31. F. Aharonian *et al.* .
32. WCDA arXive paper for Crab observation on CPC .
33. F. Aharonian, *et al.*, *Chinese Physics C* **45**, in press (2021).
34. C. C. Popescu, *et al.*, *MNRAS* **470**, 2539 (2017).
35. D. Khangulyan, F. A. Aharonian, S. R. Kelner, *ApJ* **783**, 100 (2014).
36. E. Kafexhiu, F. Aharonian, A. M. Taylor, G. S. Vila, *Phys. Rev. D* **90**, 123014 (2014).

- 37. J. E. Baldwin, *The Crab Nebula*, R. D. Davies, F. Graham-Smith, eds. (1971), vol. 46 of *IAU Symposium*, p. 22.
- 38. J. F. Macías-Pérez, F. Mayet, J. Aumont, F. X. Désert, *ApJ* **711**, 417 (2010).
- 39. E. P. Ney, W. A. Stein, *ApJ* **152**, L21 (1968).
- 40. G. L. Grasdalen, *PASP* **91**, 436 (1979).
- 41. D. A. Green, R. J. Tuffs, C. C. Popescu, *MNRAS* **355**, 1315 (2004).
- 42. T. Temim, *et al.*, *AJ* **132**, 1610 (2006).
- 43. M. P. Veron-Cetty, L. Woltjer, *A&A* **270**, 370 (1993).
- 44. G. S. Hennessy, *et al.*, *ApJ* **395**, L13 (1992).

## **4 Author Contributions**

The authors contributed to the paper in equivalent fractions.

## **5 data availability**



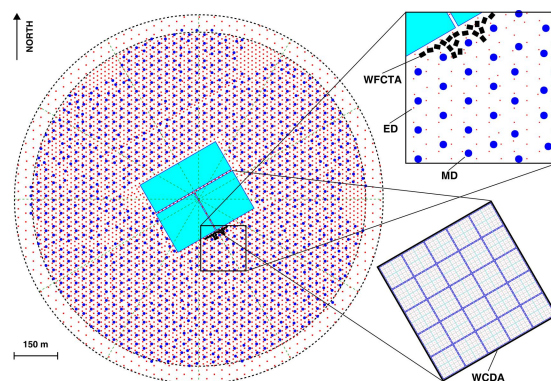


Figure S1: Schematic of the LHAASO layout (2).

## Supplementary figures

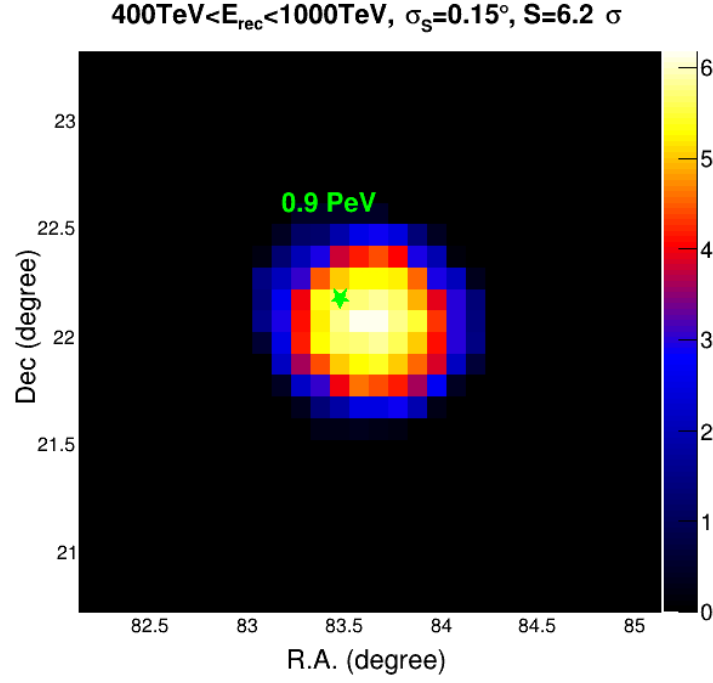


Figure S2: Significance maps centered on the Crab Nebula at energy  $> 400$  TeV.  $\sigma_S$  is the sigma of the 2-dimension Gaussian taken according to the PSF of KM2A. The color represents the significance.  $S$  is the maximum value in the map. The star marks the direction of the 0.9 PeV event.

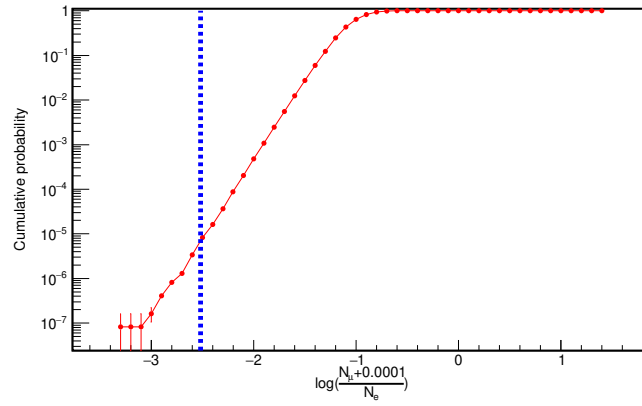


Figure S3: Distribution of events from all directions  $\pm 12^\circ$  away from the galactic plane in  $\log_{10}((N_\mu + 0.0001)/N_e)$  with a criterion of  $E_{\text{rec}} > 0.88$  PeV. In total, 12.3 million events found in the data taken in 308 days. The vertical bar indicates the ratio measured with this event, i.e. -2.52. One found very few events below the value.

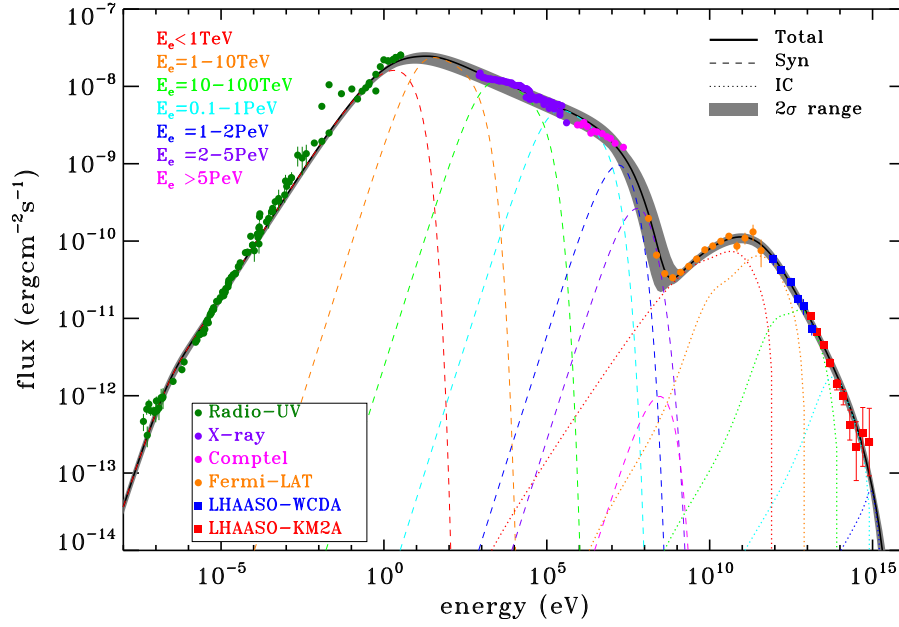


Figure S4: Crab Nebula from Radio to PeV fitted by a single electron component, with the contribution being decomposed into electrons of different energies as represented by curves of different colors. The dashed and dotted curves show the synchrotron radiation and the IC radiation of electrons with the best-fit parameters, while the black solid curve is the sum. The gray shaded region represents the  $2\sigma$  uncertainty range of the fitting. The best-fit model parameters including the  $1\sigma$  errors are  $\alpha_1 = 1.69 \pm 0.04$ ,  $\alpha_2 = 3.37 \pm 0.04$ ,  $E_b = 0.64^{+0.10}_{-0.12}$  TeV,  $E_0 = 2.45^{+1.1}_{-0.9}$  PeV,  $W_e = 6.25^{+0.5}_{-0.7} \times 10^{48}$  ergs,  $B = 115^{+6}_{-8}$   $\mu$ G. The green circles show the radio (37, 38), infrared (39–42), optical (43), and UV (44) emissions of the nebula. The light blue and purple circles are Comptel data and X-ray data from various instruments (22). The orange circles are Fermi-LAT’s observation on the non-flare state of the nebula (27). Magenta and red squares are the LHAASO (WCDA and KM2A) measurements on Crab nebula reported in this work.

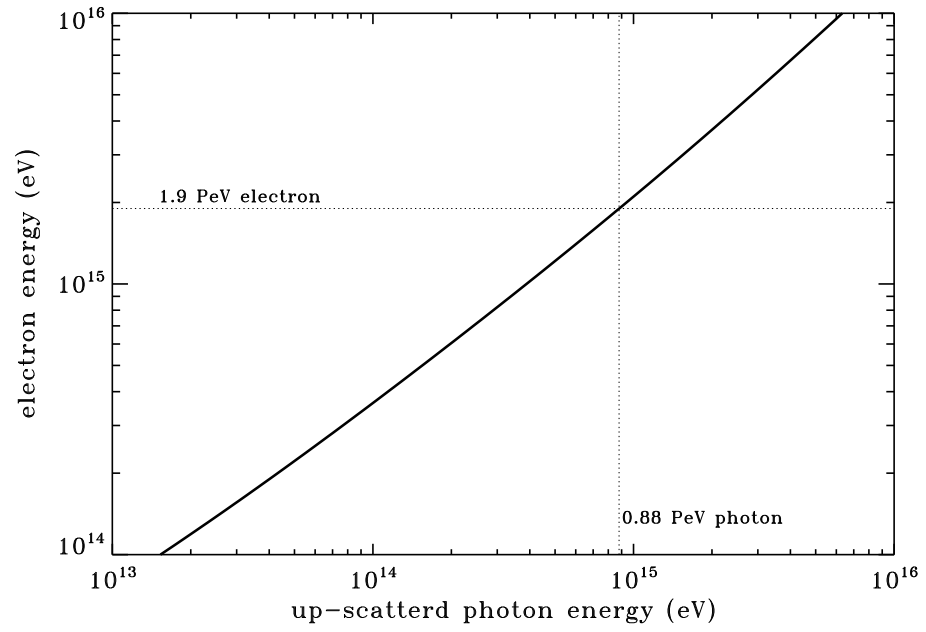


Figure S5: Relation between the average energy of up-scattered photons from the 2.7K CMBR and the energy of the scattering electrons.